Eur. Phys. J. D **15**, 257–266 (2001)

THE EUROPEAN PHYSICAL JOURNAL D

EDP Sciences

First principle theory for cavity solitons in semiconductor microresonators

L. Spinelli[1,a], G. Tissoni[1], M. Tarenghi[1], and M. Brambilla[2]

[1] INFM, Dipartimento di Scienze Chimiche, Fisiche e Matematiche, Università dell'Insubria, via Valleggio 11, 22100 Como, Italy

[2] INFM, Dipartimento di Fisica Interateneo, Università e Politecnico di Bari, via Orabona 4, 70126 Bari, Italy

Received 18 January 2001

Abstract. Cavity solitons are similar to spatial solitons, appearing as localized bright dots in the transverse intensity profile of the electromagnetic field, but they arise in dissipative systems. In this paper we consider a broad-area vertical-cavity semiconductor microresonator, driven by an external coherent field, at room temperature. The active material is constituted by a Multiple Quantum Well GaAs/AlGaAs structure (MQW). We present a set of nonlinear dynamical equations for the electric field and the carrier density valid for both a passive and an active (*i.e.* with population inversion) configuration. The complex nonlinear susceptibility is derived on the basis of a full many-body theory, with the Coulomb enhancement treated in the Padé approximation. The linear stability analysis of the homogeneous steady states is performed with a generalised approach, and numerical simulations demonstrating the existence of spatial patterns and cavity solitons in experimentally achievable parameter regions are given for the two configurations.

PACS. 42.70.Nq Other nonlinear optical materials; photorefractive and semiconductor materials – 42.65.Tg Optical solitons; nonlinear guided waves

1 Introduction

Applications to information technology are one of the goals of the extensive work in the field of transverse patterns formation in nonlinear optical systems [1–6]. The problem of the correlation among different points in an optical pattern can be solved by generating spatial structures which are localized in a portion of the transverse plane in such a way that they are individually addressable and independent from one another.

The confinement of light in short intervals of time and small regions of space is a well-known problem in nonlinear fiber optics, where temporal solitons are due to the confining action of the nonlinear material that prevents the spreading of the pulse caused by frequency dispersion. Moreover, an extensive literature on spatial solitons also exists (see *e.g.* [7,8]), where the confinement of light in localized region of the transverse plane is based on beam propagation in a nonlinear medium: in this case the nonlinearity counterbalances the spreading effect of diffraction.

In order to perform information encoding and processing, however, the usual kind of spatial solitons, based on propagation schemes, plays a marginal role in our case. As a matter of fact, the basic property of the localized structures considered in our study is that, once they have been created, for example by an address pulse, they persist as stationary dots also when the exciting pulse is removed, until they are wiped out by another suitable pulse. In this way we have a tool which allows us to exert an external control on the localized structures. This behavior is ensured by the presence of an optical cavity, a distinctive feature of our research. These localized structures are named Cavity Solitons (CS).

Pioneering work on CS has been done by Moloney *et al.* [9–11]. Solitons in cavity systems were also predicted by Rosanov [12–14] and by Mandel *et al.* [15,16], even if the mechanism underlying their formation is different. More recently, the existence of stable CS in a simple two-level model for a saturable absorber was predicted by Firth *et al.* [17], while in [18], the formation, control and interaction properties of CS were studied for the same model. Moreover, the formation of CS in photorefractively pumped ring resonators [19], in active cavities with a saturable absorber [20,21] and in quadratic nonlinear media [22,23] has been reported.

Most interesting from the practical viewpoint, for miniaturization purposes, is the case in which the active medium is a semiconductor: the standard configuration on which we will focus our attention is that of an optical cavity containing a semiconductor medium and driven by a stationary holding beam, which provides the energy to the system. Both the material sample and the holding beam have a large section.

In recent papers [24–27] a number of phenomenological simple models have been derived in order to describe the semiconductor material: more precisely, in [25–27] the

[a] e-mail: lorenzo.spinelli@uninsubria.it

active medium is assumed to be a multiple quantum well structure (MQW), with the excitonic nonlinearity modeled as a Lorentzian line. The existence and stability of CS for this model has been demonstrated, both in absence and in presence of carrier injection providing population inversion, in a wide range of the model parameters. On the other hand, a more accurate modelization of the semiconductor material, including a microscopic description of the optical nonlinearity as that given in [28,29], has been performed in [30–32]. In [32], the case of a bulk semiconductor without any injection of carriers was considered. In order to describe accurately the nonlinear response of the material from a microscopic viewpoint, the free-carrier susceptibility has been corrected by the phenomenological introduction of the two most relevant many-body effects for the operational regime considered: the band-gap renormalization and the Urbach-tail. For such a model existence and stability of CS has been theoretically predicted [33,34].

This case is interesting on the applicative side, because bulk samples are easier to grow and can be architectured with high accuracy, *e.g.* with respect to planarity requirements. Besides, theory is currently a key element in steering experiments toward a successful observation of CS in these devices [35].

In this paper we have introduced a different modelization for the case of a semiconductor medium with a MQW structure, and calculated the nonlinear susceptibility from a microscopic viewpoint [36]. In 2-D geometry, the Coulomb enhancement due to many-body effects is much more relevant at room temperature, than in the case of a bulk semiconductor [37]. We have taken into account the Coulomb enhancement by applying the *Padé* approximation [28,29] in the microscopic description of the semiconductor. Also the band-gap renormalization has been included at the same microscopic level. Moreover, the Urbach tail correction has been considered in the same way as in the bulk case.

Then, starting from the calculated nonlinear susceptibility, we have performed the numerical integration of the equations describing both field and carrier dynamics, with the aim of finding stable CS. We have considered both the passive and the active configuration: in the latter one an electric current is supplied in order to obtain population inversion in the nonlinear material. However, we have always assumed to work below the laser threshold.

In Section 2, we introduce a general model describing a vertical-cavity semiconductor microresonators. Section 3 is devoted to a detailed description of the nonlinear susceptibility $\chi_{\rm nl}$ in the case of a MQW structure. Then, the linear stability analysis is performed in Section 4, while in Section 5 some numerical results on pattern formation and CS existence are presented. Finally, Section 6 concludes this paper.

2 Vertical-cavity semiconductor microresonator

We study here a broad-area vertical-cavity semiconductor microresonator, driven by an external coherent field, at

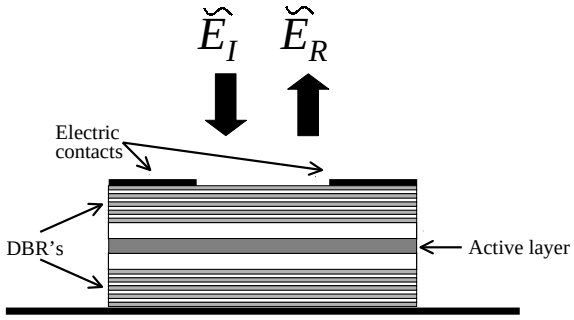

Fig. 1. Scheme of the device. The slowly varying envelopes of the injected field $\tilde{E}_{\rm I}$ and of the reflected field $\tilde{E}_{\rm R}$ are shown.

room temperature. The resonator is of the Fabry-Perot type with Distributed Bragg Reflectors (DBR), and both the reflectors and the active layers are perpendicular to the direction z of propagation of the radiation inside the cavity. The scheme of the device is depicted in Figure 1.

We consider a sample in which the active material consists of few Quantum Wells of GaAs/AlGaAs type (MQW). We speak about "active" material, referring to the semiconductor layers where the nonlinear interaction takes place. We will study both a passive configuration, in which no current is injected to create a population inversion, and an active configuration, in which an injected current causes a population inversion in the active medium, but in such a way to keep the device below the laser threshold. Typical device dimensions of interest are 100×100 μm for transverse section, a few μm for resonator length (λ-cavity), 10nm for quantum well thickness.

The basic equations governing the dynamics of the system are derived in the paraxial and slowly varying envelope approximations, mean field limit and single longitudinal mode approximation. They can be cast in the following form [26,32]:

$$\frac{\partial\tilde{E}}{\partial t} = -(1+\mathrm{i}\theta)\tilde{E} + \tilde{E}_{\rm I} + \mathrm{i}\Sigma\chi_{\rm nl}\tilde{E} + \mathrm{i}\nabla_\perp^2\ \tilde{E} \tag{1}$$

$$\frac{\partial\tilde{N}}{\partial t} = -\gamma\left[\tilde{N} + \beta\tilde{N}^2 - I - \Im(\chi_{\rm nl})|\tilde{E}|^2 - d\nabla_\perp^2\ \tilde{N}\right]. \tag{2}$$

The dynamical variables are the adimensional electric field

$$\tilde{E} = \sqrt{\frac{\epsilon_0\tau_{\rm r}L_{\rm A}}{\hbar N_0}}E, \tag{3}$$

and the normalized carrier density $\tilde{N} = N/N_0$, where ϵ_0 is the vacuum dielectric constant, $\tau_{\rm r}$ is the nonradiative recombination rate of carriers, $L_{\rm A}$ is the thickness of the active material, and N_0 is the carrier density at transparency.

$\tilde{E}_I$ is the adimensional slowly varying envelope of the field injected into the cavity, at frequency ω_0, propagating through the material at velocity $v = c/n_{\rm b}$, $n_{\rm b}$ being the background refractive index of the semiconductor. $\tilde{I}$ is the normalized injected current and will be different from zero only in the active configuration.

Time is scaled to the photon lifetime $\tau_{\rm ph} = 2L/vT$, L being the cavity length and T the mean value of the

Table 1. Typical physical values for a MQW sample based on GaAs compounds.

Cavity length	$L = 2.5\,\mu$m
Thickness of the active layer	$L_\mathrm{A} = 300$ nm
Mirror reflectivity	front: $R_\mathrm{F} = 0.995$
	back: $R_\mathrm{B} = 0.997$
Carrier nonradiative lifetime	$\tau_\mathrm{r} = 1 \div 5$ ns
Carrier diffusion length	$l_\mathrm{d} = 3\,\mu$m
Background refractive index	$n_\mathrm{b} = 3.5$

front (T_F) and back (T_B) mirror transmissivity, while the transverse coordinates x and y are scaled to the diffraction length $l_\mathrm{a} = \sqrt{\tau_\mathrm{ph} v^2 / 2\omega_0}$. The adimensional decay rate γ is the ratio between photon and carrier lifetimes $\gamma = \tau_\mathrm{ph}/\tau_\mathrm{r}$, while the quadratic term $\beta\tilde{N}^2$ is related to two-carriers radiative recombination (spontaneous emission).

The bistability parameter Σ is defined as

$$\Sigma = \frac{L_\mathrm{A}\omega_0}{n_\mathrm{b} c T}; \tag{4}$$

Σ plays essentially the same role as the parameter C of optical bistability [38,39], used in the two-level saturable absorber model [17,18].

The transverse Laplacian is defined as usual: in the field equation (1) it describes diffraction in the paraxial approximation, while in the carrier equation (2) represents carrier diffusion, with an adimensional diffusion coefficient d.

The radiation-matter interaction is described by the complex nonlinear susceptibility χ_nl, which is a function of the carrier density N and of the frequency of the injected field ω_0.

In experiments with vertical-cavity semiconductor devices, the reflected field is analyzed. Thus, if we want to compare our predictions with the experiments, we have to take into account the relation between the intracavity field and the reflected field. In our notation, the relation holding for a Fabry-Perot resonator reads [40]:

$$\tilde{E}_\mathrm{R} = \tilde{E}_\mathrm{I} - \sigma\tilde{E}, \tag{5}$$

where the parameter σ depends on the transmissivity of the front mirror: $\sigma = T_\mathrm{F}/T$. Note that if the two mirrors have the same transmissivity $\sigma = 1$. In Table 1 we report the values of some physical parameters characteristic of the samples we are dealing with.

Now we need to introduce in equations (1, 2) the explicit dependence of the nonlinear susceptibility χ_nl on the carrier density N and on the input frequency ω_0. Next section will be devoted to a detailed description of χ_nl in the MQW case. In particular, a key element will be the role of the excitonic resonance.

3 Microscopic theory for the semiconductor material

The radiation-matter interaction inside a semiconductor medium is described by the semiconductor Bloch equations [28,29]. In considering a 2-D structure, we take into account the two main many-body effects which affect the optical response of the medium.

The first one is the density-dependent contribution to the transition energy (the so-called band-gap renormalization). The second one is the renormalization of the electric-dipole interaction energy. The latter effect is responsible for the excitonic resonance that is very pronounced, also at room temperature [37].

As for the band-gap renormalization, a contribution is given by the increasingly effective plasma screening due to the increase of the carrier density. In fact, at low carrier density, the lack of vacancies in the valence band prevents the redistribution of charge in order to effectively screen the Coulomb potential. As the carrier density increases, the higher densities of holes and electrons in the valence and conduction bands, respectively, result in a more efficient screening. The term that includes this effect is called Coulomb-hole self energy $\Delta\epsilon_\mathrm{CH}$ and reads [28,29]:

$$\begin{aligned}\Delta\epsilon_\mathrm{CH} &= \sum_{q_\perp \neq 0} (V_{s,q_\perp} - V_{q_\perp}) \\ &= -\sum_{q_\perp \neq 0} V_{q_\perp} \frac{\omega_\mathrm{pl}^2}{\omega_\mathrm{pl}^2\left(1 + \frac{q_\perp}{\kappa}\right) + \frac{C}{4}\left(\frac{\hbar q_\perp^2}{2m_\mathrm{R}}\right)^2},\end{aligned} \tag{6}$$

where $q_\perp$ is the 2-D carrier momentum and we used the plasmon-pole approximation for the screened Coulomb potential

$$V_{s,q_\perp} = V_{q_\perp} \frac{\omega_\mathrm{pl}^2 \frac{q_\perp}{\kappa} + \frac{C}{4}\left(\frac{\hbar q_\perp^2}{2m_\mathrm{R}}\right)^2}{\omega_\mathrm{pl}^2\left(1 + \frac{q_\perp}{\kappa}\right) + \frac{C}{4}\left(\frac{\hbar q_\perp^2}{2m_\mathrm{R}}\right)^2}, \tag{7}$$

being $V_{q_\perp}$ the 2-D Fourier transform of the Coulomb potential; $\omega_\mathrm{pl} = \dfrac{2\pi e^2 N q_\perp}{\epsilon_0 n^2 m_\mathrm{R}}$ is the plasma frequency;

$$\kappa = \frac{2\pi \mathrm{e}^2}{\epsilon_0 n^2}\left(\frac{\partial N_\mathrm{e}}{\partial \mu_\mathrm{e}} + \frac{\partial N_\mathrm{h}}{\partial \mu_\mathrm{h}}\right)$$

is the inverse screening length.

By converting the summation over $q_\perp$ in equation (6) into an integral, one gets approximately [41]:

$$\Delta\epsilon_\mathrm{CH} = -2\epsilon_\mathrm{R} a_0 \kappa \ln\left[1 + \left(\frac{32\pi N a_0^2}{C(a_0\kappa)^3}\right)^{1/2}\right], \tag{8}$$

where ϵ_R and a_0 are the Rydberg energy and the Bohr radius of the exciton, respectively.

The other effect which renormalizes the band-gap is due to the Hartree-Fock energy correction and is

called screened-exchange shift. By considering the quasi-equilibrium approximation, it reads [28,29]:

$$\Delta\epsilon_{\rm SX} = -\sum_{q_\perp} V_{s,q_\perp}(f_{{\rm e}q_\perp} + f_{{\rm h}q_\perp}), \tag{9}$$

where the Fermi-Dirac distributions are defined as:

$$f_{\alpha q_\perp}(N) = \frac{1}{\exp\{\bar{\beta}[\epsilon_{\alpha q_\perp} - \mu_\alpha(N)]\}+1}, \tag{10}$$

the label $\alpha = {\rm e,h}$ referring to electrons and holes respectively, $\bar{\beta} = 1/k_{\rm B}T$, being $k_{\rm B}$ the Boltzmann constant and $T = 300$ K. $\mu_\alpha(N)$ is the chemical potential of electrons/holes and $\epsilon_{\alpha q_\perp} = \hbar^2 q_\perp^2/2m_\alpha$ is the electron/hole energy.

Due to these corrections, the renormalized 2-D band gap can be written as:

$$\epsilon'_{\rm gap} = \epsilon^{\rm (2D)}_{\rm gap} + \Delta\epsilon_{\rm CH} + \Delta\epsilon_{\rm SX}\,. \tag{11}$$

As for the Coulomb-enhancement, we adopt the Padé approximation in resolving the semiconductor Bloch equations [41,42]. In the quasi-equilibrium approximation, the expression of the complex susceptibility which describes the radiation-matter interaction reads [29]:

$$\chi(N,\omega_0) = -\frac{\rm i}{\epsilon_0\hbar V_{\rm A}}\sum_{k_\perp}\frac{|\mu_{k_\perp}|^2}{1-q(k_\perp)}\frac{f_{{\rm e}k_\perp}(N)+f_{{\rm h}k_\perp}(N)-1}{{\rm i}(\omega_{k_\perp}-\omega_0)+\gamma_{k_\perp}}\,. \tag{12}$$

$\mu_{k_\perp}$ is the dipole matrix element between the valence and the conduction band, calculated in [43,44]:

$$|\mu_{k_\perp}|^2 = \frac{\epsilon^{\rm (2D)}_{\rm gap}\left(\epsilon^{\rm (2D)}_{\rm gap}+\Delta_{\rm s}\right)}{4\left(\epsilon^{\rm (2D)}_{\rm gap}+2\Delta_{\rm s}/3\right)}\left(\frac{1}{m_{\rm e}}-\frac{1}{m_0}\right)\left(\frac{e\hbar}{\hbar\omega_{k_\perp}}\right)^2, \tag{13}$$

$\hbar\omega_{k_\perp} = \epsilon'_{\rm gap} + \hbar^2 k_\perp^2/2m_{\rm R}$ is the transition energy at the carrier momentum $k_\perp$, $m_{\rm R}$ being the electron/heavy-hole reduced mass; $V_{\rm A}$ is the active volume; the Fermi-Dirac distributions are defined in equation (10). Moreover, in order to correct the overestimation of the effects of homogeneous broadening because of the slowly decaying tails of Lorentzian functions, leading to an excessive absorption at photon frequencies below the band gap, we have considered an exponential dependence on $k_\perp$ in the polarization decay rate $\gamma_{k_\perp}$:

$$\gamma_{k_\perp} = \frac{2\gamma_{\rm p}}{\exp\left(\frac{\hbar\omega_k-\hbar\omega_0}{E_0}\right)+1}, \tag{14}$$

where $\gamma_{\rm p}$ and E_0 are phenomenological parameters [44]. This assumption restores the exponential decay for frequencies below the band gap, which appears in experimental spectra and is known as the Urbach tail of the electron-hole resonances in semiconductors.

The factor $[1-q(k_\perp)]^{-1}$ represents the Coulomb enhancement in the Padé approximation [29]; it results:

$$q(k_\perp) = \frac{1}{\mu_{k_\perp}}\sum_{k'_\perp\neq k_\perp} V_{s,|k'_\perp-k_\perp|}\chi^{(0)}_{k'_\perp}, \tag{15}$$

where

$$\chi^{(0)}_{k_\perp} = -\frac{{\rm i}\mu_{k_\perp}}{\hbar}\frac{f_{{\rm e}k_\perp}(N)+f_{{\rm h}k_\perp}(N)-1}{{\rm i}(\omega_{k_\perp}-\omega_0)+\gamma_{k_\perp}}\,. \tag{16}$$

As usual, the imaginary part of the complex susceptibility is related to absorption, while the real part of (12) contains the information related to the refractive index change due to the presence of the electric field. More precisely, since the contribution to the refractive index at zero-carriers is already included in the background lattice refractive index $n_{\rm b}$, we describe the effective carrier-induced refractive index change δn by introducing the nonlinear susceptibility $\chi_{\rm nl}$ [45]. As for its real part, it is defined as:

$$\Re[\chi_{\rm nl}(N,\omega_0)] = \Re[\chi(N,\omega_0)] - \Re[\chi(0,\omega_0)]. \tag{17}$$

The Padé approximation, however, holds provided we consider carrier densities above the Mott-density [28], that for the devices we are dealing with is about 10^{11} cm^{-2}. In order to evaluate the complex susceptibility at zero-carriers density in equation (17) we decided to perform a linear extrapolation from the values calculated at larger densities.

On the contrary, the imaginary part of $\chi_{\rm nl}$ coincides with that of the complex susceptibility (12).

The relations linking the real and imaginary part of $\chi_{\rm nl}$ to the refractive index change δn and the intensity absorption coefficient $\bar{\alpha}$, respectively, are the following [29]:

$$\delta n = \frac{1}{2n_{\rm b}}\Re(\chi_{\rm nl}); \quad \bar{\alpha} = \frac{\omega_0}{n_{\rm b}c}\Im(\chi_{\rm nl}). \tag{18}$$

The summations in equations (9, 12, 15) can be calculated numerically, by following an ordinary procedure of converting them into integrals (see for example [29]).

We devoted an initial phase of our research to the optimization of the various parameters present in the model, in order to match the theoretical results with the experimental evidences. In particular, we set the parameters in such a way to have the excitonic peak at about 1.46 eV with a width of about 4 meV, as it results from absorption spectra for GaAs MQW structures, at room temperature (see for example Ref. [37]).

Then, we are able to show in Figure 2 the calculated refractive index change δn (a) and the absorption coefficient $\bar{\alpha}$ (b), for the MQW case, as functions of the input photon energy. In these plots we have also introduced the adimensional band-gap detuning parameter Δ defined as:

$$\Delta = (\epsilon^{\rm 2D}_{\rm gap} - \hbar\omega_0)/4\epsilon_{\rm R}, \tag{19}$$

where $\epsilon_{\rm R}$ is the excitonic Rydberg energy (the factor 4 is present because we are dealing with a 2-D geometry).

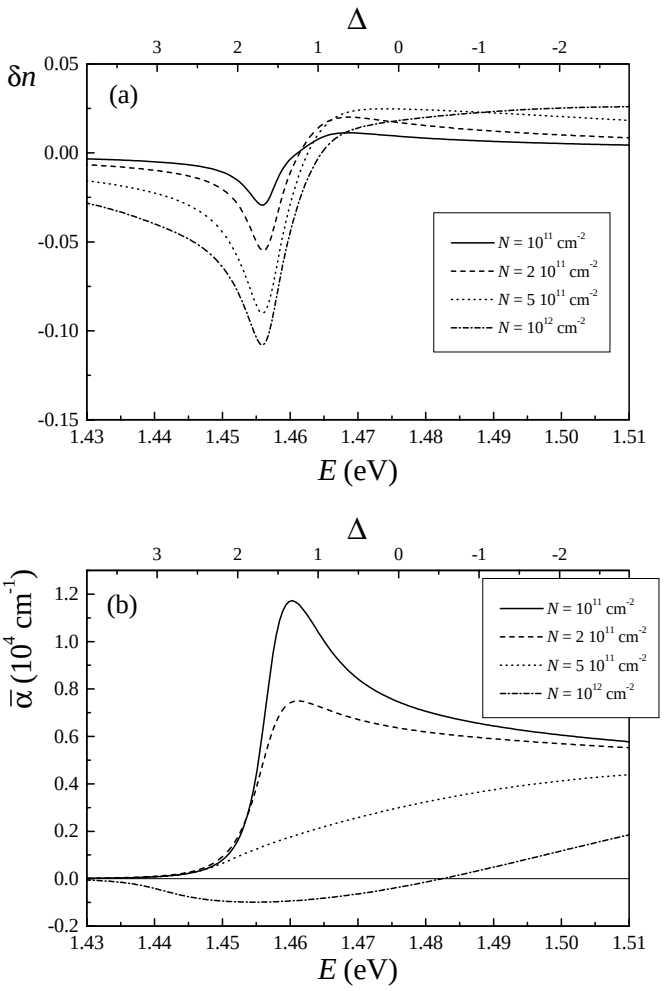

Fig. 2. Refractive index variation (a) and absorption coefficient (b) as functions of the input photon energy and of the band-gap detuning parameter Δ, for different values of the carrier density N.

From the absorption spectra reported in Figure 2b, we can observe the presence of the excitonic resonance due to the Coulomb enhancement. The spectra obtained with our calculation of the nonlinear susceptibility in the MQW case are comparable with similar spectra present in literature [28,46]. For the limitation of the Padé approximation stated above, we show absorption spectra for $N \geq 10^{11}$ cm^{-2}.

We note that the excitonic peaks obtained in experimental spectra (see for example Ref. [37]) appear sharper for very low illuminating power: they correspond to very low carrier densities, where we can not apply the Padé approximation. Moreover, in the absorption spectrum reported in reference [37] for GaAs MQW structure at room temperature, it is evident the presence of the light-hole excitonic peak, that we have not included in our model.

In order to have a check for the refractive index change and the absorption coefficient reported above, we have also performed the calculation of the refractive index change δn in a different way, by exploiting the Kramers-Kronig relations which link the real and imaginary parts of the

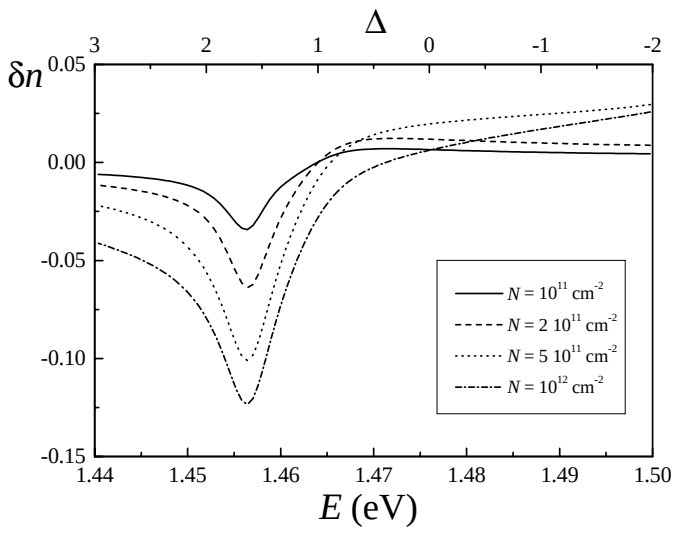

Fig. 3. Refractive index variation as functions of the input photon energy and of the band-gap detuning parameter Δ, for different values of the carrier density N, obtained by means of the Kramers-Kronig transformation of the absorption coefficient α reported in Figure 2b.

complex susceptibility. In particular, taking into account equation (18), we can write the Kramers-Kronig relation in the following form:

$$\delta n(\omega) = \frac{2c}{\pi} P.P. \int_0^{+\infty} \frac{\delta\bar{\alpha}(\omega')}{\omega'^2 - \omega^2} \mathrm{d}\omega'. \qquad (20)$$

In Figure 3 we report the refractive index change δn as a function of the input photon energy, for different values of the carrier density N, calculated from equation (20), where we used the previously determined absorption coefficient $\bar{\alpha}$ (see Fig. 2b). As a matter of fact there is a very good agreement between this curves and those reported in Figure 2a.

In the active configuration the device becomes an amplifier. Then, we have to consider the gain, instead of the absorption, spectra and the linewidth enhancement factors: they can be calculated from the nonlinear susceptibility χ_{nl}, resulting:

$$g = -\frac{\omega_0}{n_{\mathrm{b}} c} \Im(\chi_{\mathrm{nl}}); \quad \alpha = \frac{\partial \Re(\chi_{\mathrm{nl}})/\partial N}{\partial \Im(\chi_{\mathrm{nl}})/\partial N}, \qquad (21)$$

where g and α are the gain coefficient and the linewidth enhancement factor, respectively. In Figure 4 are presented the calculated gain coefficients and α-factors as functions of the input photon energy. Again, these quantities are comparable with similar spectra present in literature [29].

The expression (12) for the nonlinear susceptibility χ_{nl} will be the basis for the analysis of a microresonator with a MQW active layer presented in following sections.

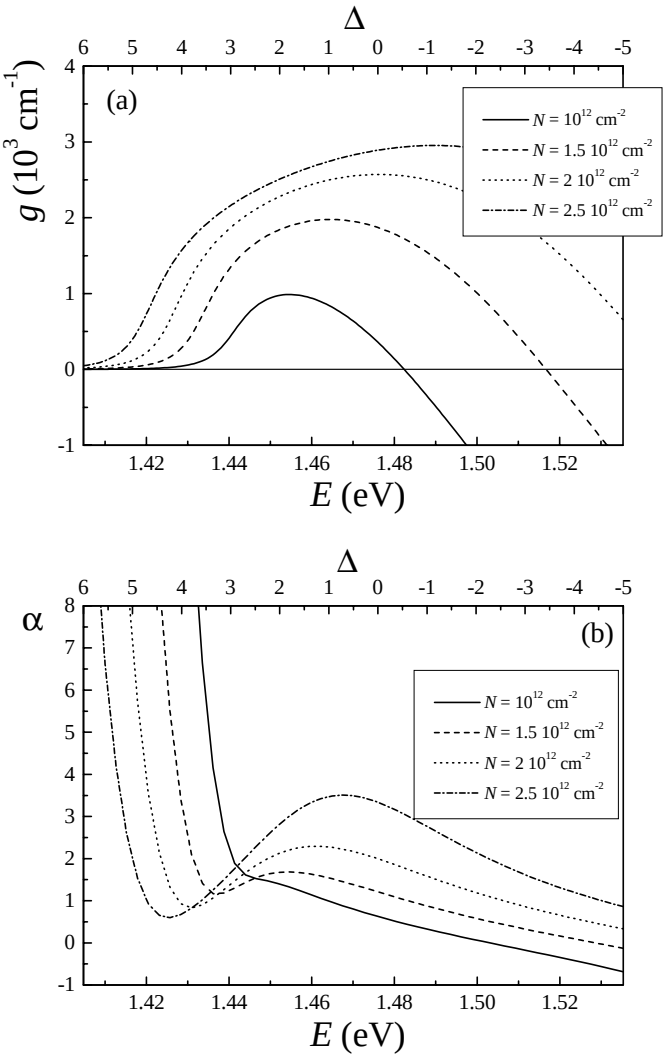

Fig. 4. Active configuration. Gain coefficient g (a) and linewidth enhancement factor (b) as functions of the input photon energy and of the band-gap detuning parameter Δ, for different values of the carrier density N.

4 Homogeneous steady state and linear stability analysis

The homogeneous solution $(E_{\rm S}, N_{\rm S})$ of equations (1, 2) (hereafter we will omit the tilde for E and N) is obtained by setting to zero all the temporal and spatial derivatives. We obtain

$$|E_{\rm I}|^2 = |E_{\rm S}|^2 \left\{ [1+\Sigma\Im(\chi_{\rm nl})]^2 + [\theta-\Sigma\Re(\chi_{\rm nl})]^2 \right\}, \quad (22)$$

$$|E_{\rm S}|^2 = \frac{N_{\rm S} + \beta N_{\rm S}^2 - I}{\Im(\chi_{\rm nl})}. \quad (23)$$

In the active configuration the nonlinear material acts as an amplifier, and in order to determine the laser threshold $I^{\rm th}$, we have to additionally set $E_{\rm I} = E = 0$ in equations (1, 2). In fact, we are interested in the condition for which the intracavity field E starts to become different from zero, when the driving field $E_{\rm I}$ is not present. Actually, intracavity field is different from zero also below threshold, due to spontaneous emission. In our model, however, we consider spontaneous emission in the lasing mode as a negligible effect. Then, from equation (1) we have the condition:

$$\Sigma\Im\left[\chi_{\rm nl}(N^{\rm th})\right] + 1 = 0, \quad (24)$$

giving the value of the carrier density at threshold $N^{\rm th}$. Then, from equation (2), we obtain the value of the laser threshold:

$$I^{\rm th} = N^{\rm th} + \beta\left(N^{\rm th}\right)^2. \quad (25)$$

As we said before, in the active configuration we will always consider the laser below threshold.

For appropriate choices of the parameters, the curves of $|E_{\rm S}|$ as a function of $|E_{\rm I}|$ are S-shaped. This behavior is reflected by the shape of the $|E_{\rm R}|$ *vs.* $|E_{\rm I}|$ curves (examples are depicted in the following section).

Now, we want to study the instabilities of the homogeneous steady state, giving rise to a spatially modulated pattern (Modulational Instability). To this aim, we perform the linear stability of the homogeneous solution, by studying the response of the system to small spatially modulated fluctuations of wavevector $\mathbf{K}$ around the steady state. The eigenvalue λ satisfies the cubic equation [27,32]:

$$\lambda^3 + a_2\lambda^2 + a_1\lambda + a_0 = 0\,, \quad (26)$$

where the coefficients a_i, $i = 0, 1, 2$ depend on the system parameters β, γ, θ, d, Σ, $E_{\rm I}$ and on the modulus square K^2 of the transverse wavevector in the following way:

$$a_2 = 2A_1 + \gamma(A_4 + dK^2)\,, \quad (27)$$

$$a_1 = A_1^2 + (A_2+K^2)^2 + \gamma\left[2A_1(A_4+dK^2) + A_3\frac{\partial\Im(\chi_{\rm nl})}{\partial N}\right], \quad (28)$$

$$a_0 = \gamma\left\{\left[A_1^2 + \left(A_2+K^2\right)^2\right]\left(A_4+dK^2\right) - A_3\left[\left(A_2+K^2\right)\frac{\partial\Re\left(\chi_{\rm nl}\right)}{\partial N} - A_1\frac{\partial\Im\left(\chi_{\rm nl}\right)}{\partial N}\right]\right\}, \quad (29)$$

with

$$A_1 = 1 + \Sigma\Im(\chi_{\rm nl}), \quad (30)$$

$$A_2 = \theta - \Sigma\Re(\chi_{\rm nl}), \quad (31)$$

$$A_3 = 2\Sigma|E_{\rm S}|^2\Im(\chi_{\rm nl}), \quad (32)$$

$$A_4 = 1 + 2\beta N_{\rm S} - |E_{\rm S}|^2\frac{\partial\Im(\chi_{\rm nl})}{\partial N}. \quad (33)$$

Equation (26) usually has one real and two complex conjugate roots. The two complex eigenvalues might in principle give rise to a Hopf instability. However, it is easy to show that, since $\gamma \ll 1$, the real part of these eigenvalues is equal to $-A_1$, which is always negative. Thus there are no instabilities related to the complex eigenvalues.

The instability associated with the real eigenvalue is called Turing or stationary instability because it brings the system to a new stationary state, different from the homogeneous one. The system passes from the stable to the unstable domain when the real eigenvalue changes its sign from negative to positive. Therefore, the stability boundary is assigned by the condition $\lambda = 0$, which is in turn equivalent to $a_0 = 0$.

5 Numerical results

Now, we calculate the homogeneous steady states and the extension of the Modulational Instability domains in the parameter space. Then, we integrate numerically the dynamical equations (1, 2), by means of a split-step code with periodic boundary conditions. This method consists in separating the algebraic and the Laplacian terms in the right-hand side of the equations: the algebraic term is integrated using a Runge-Kutta algorithm, while for the Laplacian operator a 2-D FFT is adopted [47]. This implies that the number of points for each side of the grid must be a power of 2.

We split our analysis in considering the passive and the active configuration separately. For each one of these cases we choose the parameters in order to be as close as possible to the experimental feedback we receive from our partners in the European Project PIANOS (see Acknowledgements) and, simultaneously, to fulfill the empirical conditions for CS observation stated in a previous work [27].

Passive case

For this configuration, we have considered three operating regimes: the first one is $\Delta = 3$, that is, an input frequency below the excitonic resonance; the second one is $\Delta = 1$, that is close to the excitonic resonance; the last one is $\Delta = -3$, that is well in the continuum of the absorption spectrum.

Starting from the analysis of the instabilities affecting the system, presented in Figure 5, for each one of the previous cases we considered the set of parameters that seem most favorable to observe CS.

In Figure 6 we report the bistability curves with a complete characterization of the spatial patterns arising as self-organized structures. We note that there are extended branches of CS (that in the case of reflection will appear as dark spot on a brighter background), in all the presented cases. However, the relative extension of these branches with respect to the intensity of the holding beam is larger for the cases $\Delta = 1$ and $\Delta = -3$. The parameter σ was chosen as 1.5, that is we have assumed that the transmission of the front mirror is larger than that of the back mirror, as it happens in actual devices. As a general remark, we note that values of σ greater than 1 are beneficial in order to enhance the contrast of the spatial patterns.

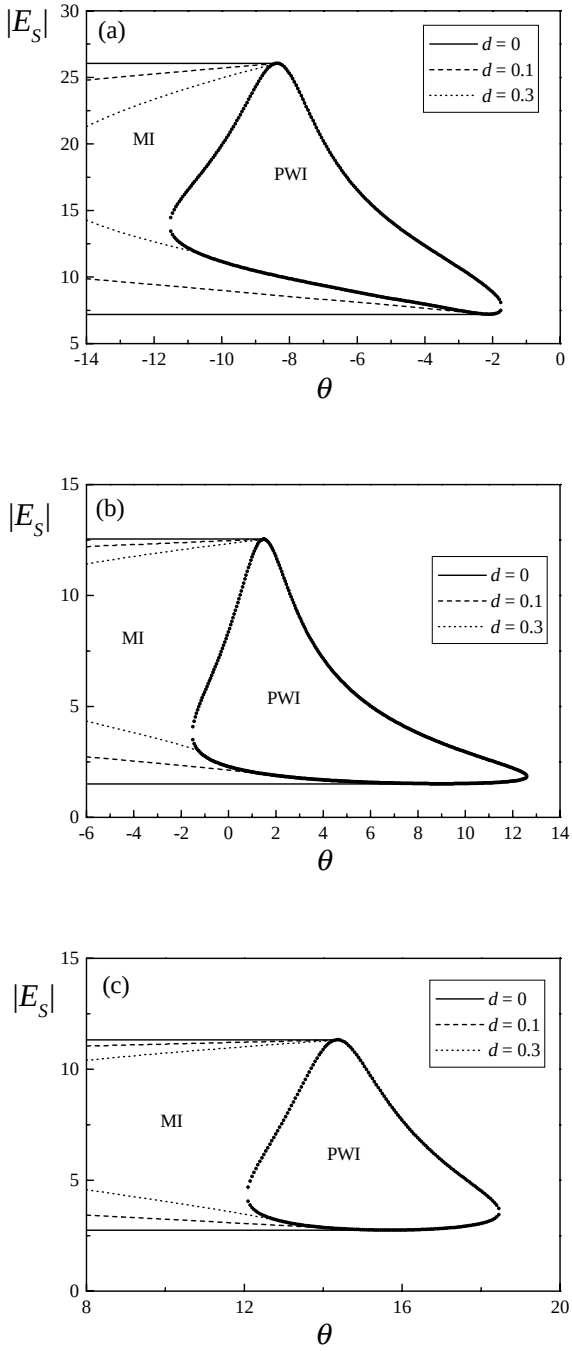

Fig. 5. Passive configuration. Plane-wave instability (PWI) and modulational instability (MI) as functions of θ, for different parameters: (a) $\Delta = 3$, $\Sigma = 80$, $\beta = 0$; (b) $\Delta = 1$, $\Sigma = 100$, $\beta = 0.5$; (c) $\Delta = -3$, $\Sigma = 80$, $\beta = 1$.

Active case

In this configuration, the microresonator is supplied with an electrical current in order to create a population inversion in the active material. In this condition the device becomes an amplifier. From analysis of plots like those reported in Figure 7a for the case $\Delta = 3$, we found that extended regions of plane-wave and modulational instabilities are present only for values of $\Delta \gtrsim 2.5$, that is, the

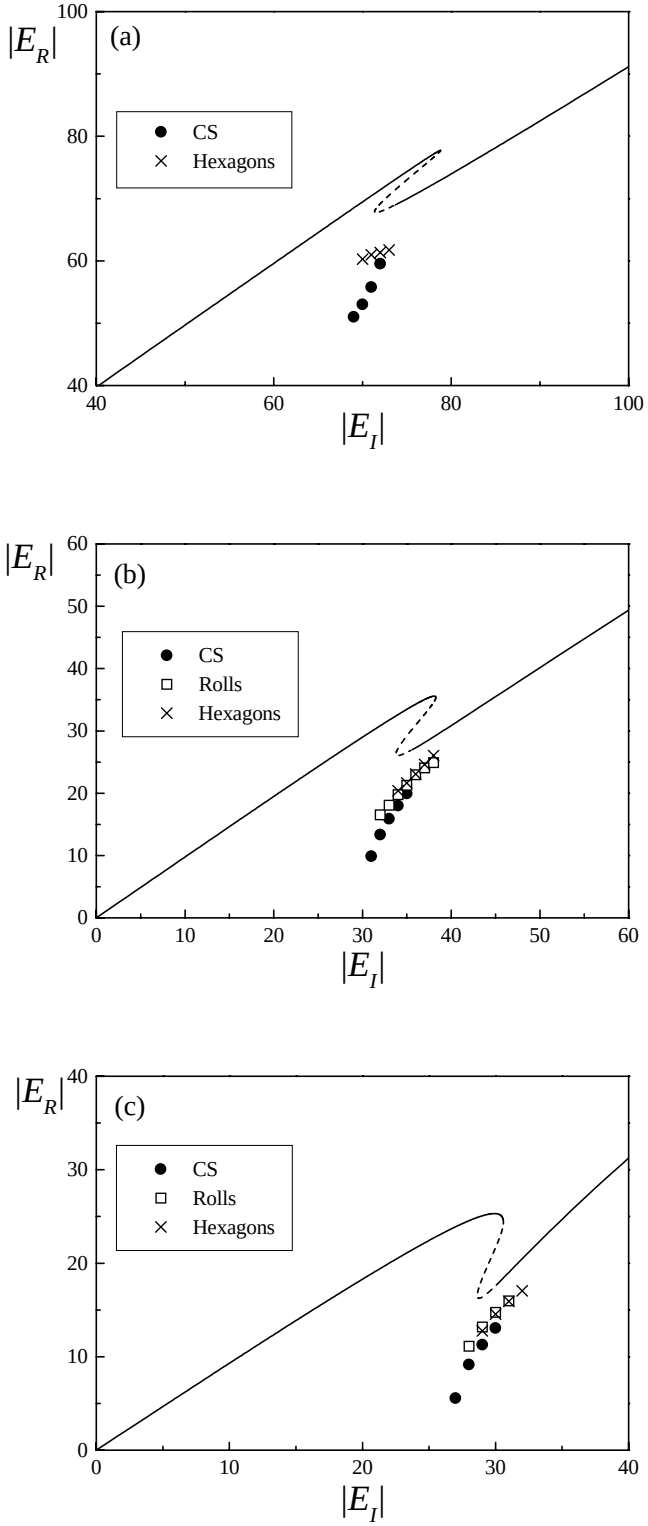

Fig. 6. Passive configuration. S-shaped homogeneous steady-state curves (dashed line indicates unstable part) of the reflected field as a function of the injected field. Also the branches of different stationary spatial structures are reported (it is plotted the value of the field at the minimum of intensity). The parameters are: (a) $\Delta = 3$, $\Sigma = 80$, $\theta = -10$, $\beta = 0$, $d = 0.3$; (b) $\Delta = 1$, $\Sigma = 100$, $\theta = 0$, $\beta = 0.5$, $d = 0.2$; (c) $\Delta = -3$, $\Sigma = 80$, $\theta = 13$, $\beta = 1$, $d = 0.1$. The parameter σ is fixed to 1.5.

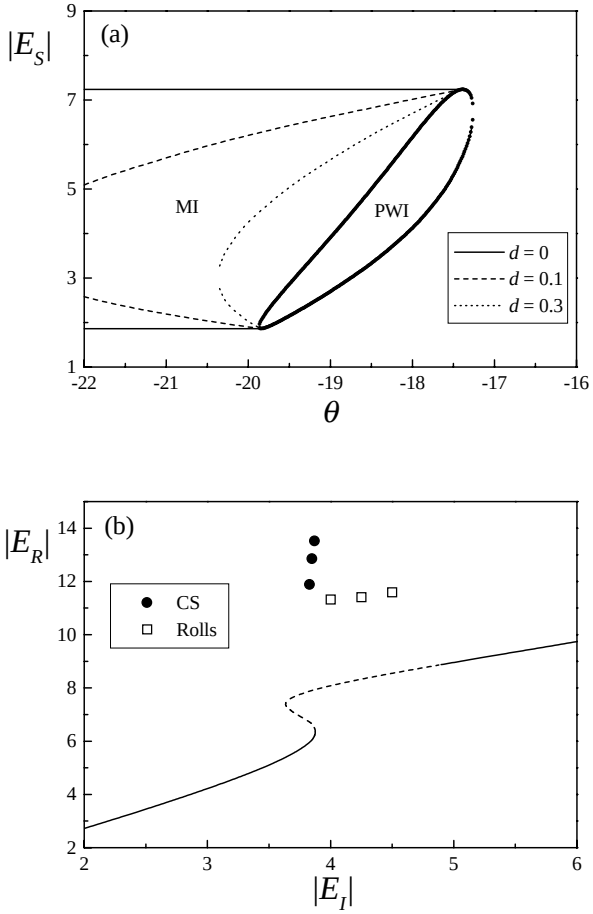

Fig. 7. Active configuration. (a) Plane-wave instability (PWI) and modulational instability (MI) as functions of θ; (b) bistable homogeneous steady-state curve (dashed line indicates unstable part) of the reflected field as a function of the injected field. The branches of different stationary spatial structures are reported (it is plotted the value of the field at the maximum of intensity). The parameters are: $\Delta = 3$, $\Sigma = 80$, $\theta = -18.5$, $\beta = 0$, $I = 1.3$, $d = 0.3$ and $\sigma = 2$. The value of the current at the laser threshold is $I^{\rm th} = 1.33$.

frequency range of the driving field must be red-shifted with respected to the gain peak. This corresponds to have an α-factor larger than approximately 3 (see Fig. 4b). This agrees with what we predicted in a previous paper, where we described the MQW structure by a simpler model [26]. In Figure 7b we report the bistability curve and the spatial pattern scenario for the case $\Delta = 3$. We observe that also in this configuration the CS are present (in this case CS appears as bright spot also in reflection), even if the extension of their branch is much smaller than in the passive case. Also this feature is a confirmation of what we already observed for the active configuration with the simpler model [26].

6 Conclusions

In this paper we studied a broad-area vertical-cavity semiconductor microresonator, driven by an external coherent

field, at room temperature. We focussed our attention to a sample in which the active material consists of GaAs/AlGaAs MQW structure. The resonator is of the Fabry-Perot type with DBR as mirrors, and we described the dynamics of the intracavity electric field and the carrier density by means of a set of partial differential equations, in which we included the transverse spatial effects, considering field diffraction and carrier diffusion, through the Laplacian operator in the paraxial approximation.

The radiation-matter interaction which takes place in the active material was modelized through the nonlinear susceptibility calculated from a microscopic viewpoint. In our modelization we take into account the two main many-body effects which are present in 2-D geometry: the Coulomb enhancement, by performing the *Padé* approximation in the microscopic description of the semiconductor; and the band-gap renormalization, included at the same microscopic level. Moreover, the Urbach tail correction was considered.

After a detailed study devoted to the optimization of the parameters included in the microscopic model, in such a way to approach experimental results, we were able to calculate absorption/gain spectra for such a kind of structures, where the presence of the excitonic peak due to the Coulomb enhancement was clearly evident.

Then, adopting the calculated nonlinear susceptibility, we performed the numerical integration of the dynamical equations, in order to analyze the transverse spatial structures exhibited by this devices. In particular we directed our research to find stable Cavity Solitons. In our analysis, we considered both a passive and an active configuration. In the latter one, an external current is supplied to the device, in order to get population inversion in the active material. Moreover, we study the electric field emitted in reflection, because this is the usual configuration adopted in experimental set-ups.

In the passive configuration, we were able to find large regions in the parameter space where CS are stable, in agreement with the "empirical conditions" for the observation of CS stated in reference [27]. Moreover, we note how, when we operate with the external frequency close to the excitonic peak, the best conditions for CS observation imply cavity resonance. Also in the active configuration we find stable CS, but the extensions of the stable branches are smaller than in the passive case. These results agree with a previous work, where the MQW structure was described by a simpler model, which considered only a Lorentzian resonance for the excitonic peak in the passive case and the linewidth enhancement factor α in the active case [26].

The theory developed in this and previous works is a key element in steering to a successful observation of CS current experiments in semiconductor microresonators. This experiments are in progress in different European Labs (CNET and INLN, France, PTB, Germany) in the framework of the European Project PIANOS (Processing of Information with Arrays of Nonlineal Optical Solitons). The experimental observation of CS in semiconductor devices would be a real breakthrough, due to the possibility of exploiting them as binary units for all-optical information treatment. Some results towards theory/experiment agreement have been already obtained in the case of the passive configuration [35], while there are recent and very promising experimental results about the observation of spatial patterns and CS in active configuration [48].

A further development of the theory will include the thermal effects, that in semiconductor devices, in some conditions, play a fundamental role [49]. Somehow, they can be avoided by operating in the pulsed regime, due to the slow temperature dynamics, but a progress of the theory in this direction is necessary and some preliminary steps have been already done [50].

This work was carried out in the framework of the ESPRIT LTR Project PIANOS "Processing of Information with Arrays of Nonlinear Optical Solitons" and of the European Program HP-RTN Network VISTA "VCSELs for Information Society Technology Applications". We thank our partners in PIANOS and their collaborators, for useful discussions and for exchanging information about preliminary experimental results.

References

1. F.T. Arecchi, Physica D **51**, 450 (1991).
2. L.A. Lugiato, Phys. Rep. **219**, 293 (1992).
3. C.O. Weiss, Phys. Rep. **219**, 311 (1992).
4. L.A. Lugiato, Chaos Solitons Fractals **4**, 1251 (1994).
5. W.J. Firth, Pattern formation in passive nonlinear optical systems, in *Self-organization in optical systems and applications in information technology*, edited by M.A. Vorontsov, W.B. Miller (Springer–Verlag, 1995), pp. 69–96.
6. L.A. Lugiato, M. Brambilla, A. Gatti, Optical Pattern Formation, in *Advances in Atomic, Molecular and Optical Physics*, edited by B. Bederson, H. Walther (Academic Press, 1998), Vol. 40, pp. 229–306.
7. P.V. Mamyshev, A. Villeneuve, G.I. Stegeman, J.S. Aitchison, Electron. Lett. **30**, 726 (1994).
8. B. Crosignani, M. Segev, D. Eugin, P. Di Porto, A. Yariv, G. Salamo, J. Opt. Soc. Am. B **10**, 446 (1993).
9. J.V. Moloney, H.M. Gibbs, Phys. Rev. Lett. **48**, 1607 (1982).
10. D.W. Mc Laughlin, J.V. Moloney, A.C. Newell, Phys. Rev. Lett. **51**, 75 (1983).
11. J.V. Moloney, H. Adachihara, D.W. Mc Laughlin, A.C. Newell, Fixed points and chaotic dynamics of an infinite-dimensional map, in *Chaos Noise and Fractals*, edited by R. Pike, L.A. Lugiato (Hilger, Bristol, 1987), pp. 137–186.
12. N.N. Rosanov, G.V. Khodova, Opt. Spectrosc. **65**, 449 (1988).
13. N.N. Rosanov, J. Opt. Soc. Am. B **7**, 1057 (1990).
14. N.N. Rosanov, Transverse patterns in wide-aperture nonlinear optical systems, in *Progress in Optics*, edited by E. Wolf (North–Holland, Amsterdam, 1996), Vol. XXXV, pp. 1–60.
15. M. Tlidi, P. Mandel, R. Lefever, Phys. Rev. Lett. **73**, 640 (1994).
16. M. Tlidi, P. Mandel, Chaos Solitons Fractals **4**, 1475 (1994).

17. W.J. Firth, A.J. Scroggie, Phys. Rev. Lett. **76**, 1623 (1996).
18. M. Brambilla, L.A. Lugiato, M. Stefani, Europhys. Lett. **34**, 109 (1996); Chaos **6**, 368 (1996).
19. M. Saffman, D. Montgomery, D.Z. Anderson, Opt. Lett. **19**, 518 (1994).
20. V.Yu. Bazhenov, V.B. Taranenko, M.V. Vasnetsov, Proc. SPIE **1806**, 14 (1992).
21. V.B. Taranenko, K. Staliunas, C.O. Weiss, Phys. Rev. A **56**, 1582 (1997).
22. K. Staliunas, V.J. Sanchez-Morcillo, Opt. Commun. **139**, 306 (1997).
23. C. Etrich, U. Peschel, F. Lederer, Phys. Rev. Lett. **79**, 2454 (1997).
24. D. Michaelis, U. Peschel, F. Lederer, Phys. Rev. A **56**, R3366 (1997).
25. M. Brambilla, L.A. Lugiato, F. Prati, L. Spinelli, W.J. Firth, Phys. Rev. Lett. **79**, 2042 (1997).
26. L. Spinelli, G. Tissoni, M. Brambilla, F. Prati, L.A. Lugiato, Phys. Rev. A **58**, 2542 (1998).
27. L.A. Lugiato, L. Spinelli, G. Tissoni, M. Brambilla, J. Opt. B: Quant. Semiclass. Opt. **1**, 43 (1999).
28. H. Haug, S.W. Koch, *Quantum Theory of the Optical and Electronic Properties of Semiconductors*, 2nd edn. (World Scientific Publ., Singapore, 1993).
29. W.W. Chow, S.W. Koch, M. Sargent III, *Semiconductor-Laser Physics* (Springer Verlag, Berlin Heidelberg, 1994).
30. D. Michaelis, U. Peschel, F. Lederer, Opt. Lett. **23**, 337 (1998).
31. D. Michaelis, U. Peschel, F. Lederer, Chaos Solitons Fractals **10**, 905 (1999).
32. G. Tissoni, L. Spinelli, M. Brambilla, T. Maggipinto, I.M. Perrini, L.A. Lugiato, J. Opt. Soc. Am. B **16**, 2083 (1999).
33. G. Tissoni, L. Spinelli, M. Brambilla, T. Maggipinto, I.M. Perrini, L.A. Lugiato, J. Opt. Soc. Am. B **16**, 2095 (1999).
34. T. Maggipinto, M. Brambilla, G.K. Harkness, W.J. Firth, Phys. Rev. E **62**, 8726 (2000).
35. R. Kuszelewicz, I. Ganne, G. Slekys, I. Sagnes, M. Brambilla, Phys. Rev. Lett. **84**, 6006 (2000).
36. M. Brambilla, L.A. Lugiato, T. Maggipinto, L. Spinelli, G. Tissoni, Proc. SPIE **3944**, 230 (2000).
37. D.S. Chemla, D.A.B. Miller, P.W. Smith, A.C. Gossard, W. Wiegmann, IEEE J. Quant. El. **QE–20**, 265 (1984).
38. R. Bonifacio, L.A. Lugiato, Lett. Nuovo Cimento **21**, 505 (1978).
39. H.M. Gibbs, *Optical Bistability: Controlling Light with Light* (Academic Press, New York, 1985).
40. M.J. Collett, C.W. Gardiner, Phys. Rev. A **30**, 1386 (1984).
41. H. Haug, S.W. Koch, Phys. Rev. A **39**, 1887 (1987).
42. P.R. Gaves-Morris, *Padé approximations and their application* (Academic Press, New York, 1973).
43. G.P. Bava, P. Debernardi, A. Pisoni, "QW optical response including valence band mixing and many body effects", Internal Rep. DE/GE 91–002, Politecnico di Torino, Turin, Italy, 1993.
44. K.W. Boer, *Survey of semiconductor physics* (Van Nostrand Reinhold, New York, 1990).
45. S.W. Koch, N. Peyghambarian, H.M. Gibbs, J. Appl. Phys. **63**, R1 (1988).
46. C. Ell, R. Blank, S. Benner, H. Haug, J. Opt. Soc. Am. B **16**, 2006 (1989).
47. W.H. Press, B.P. Flannery, S.A. Teukolsky, W.T. Vetterling, *Numerical Recipes* (Cambridge University Press, Cambridge, 1986).
48. J. Tredicce, PIANOS Internal Report, 2000.
49. C.Z. Ning, R.A. Indik, J.V. Moloney, J. Opt. Soc. Am. B **12**, 1993 (1995); T. Rossler, R.A. Indik, G.K. Harkness, J.V. Moloney, C.Z. Ning, Phys. Rev. A **58**, 3279 (1998).
50. G. Tissoni, L. Spinelli, L.A. Lugiato, M. Brambilla, Proc. SPIE (2001, to appear).